Low-Frequency Interlayer Raman Modes to Probe Interface of Twisted Bilayer MoS2

Shengxi Huang,[†] Liangbo Liang,[‡,§] Xi Ling,[*,†] Alexander A. Puretzky,[§] David B. Geohegan,[§] Bobby G. Sumpter,[§,∥] Jing Kong,[†] Vincent Meunier,[*,‡] and Mildred S. Dresselhaus[*,†,⊥]

[†]Department of Electrical Engineering and Computer Science, Massachusetts Institute of Technology, Cambridge, Massachusetts 02139, United States

[‡]Department of Physics, Applied Physics, and Astronomy, Rensselaer Polytechnic Institute, Troy, New York 12180, United States

[§]Center for Nanophase Materials Sciences and [∥]Computer Science and Mathematics Division, Oak Ridge National Laboratory, Oak Ridge, Tennessee 37831, United States

[⊥]Department of Physics, Massachusetts Institute of Technology, Cambridge, Massachusetts 02139, United States

S *Supporting Information*

ABSTRACT: van der Waals homo- and heterostructures assembled by stamping monolayers together present optoelectronic properties suitable for diverse applications. Understanding the details of the interlayer stacking and resulting coupling is crucial for tuning these properties. We investigated the low-frequency interlayer shear and breathing Raman modes (<50 cm^{-1}) in twisted bilayer MoS2 by Raman spectroscopy and first-principles modeling. Twisting significantly alters the interlayer stacking and coupling, leading to notable frequency and intensity changes of low-frequency modes. The frequency variation can be up to 8 cm^{-1} and the intensity can vary by a factor of ~5 for twisting angles near 0° and 60°, where the stacking is a mixture of high-symmetry stacking patterns and is thus sensitive to twisting. For twisting angles between 20° and 40°, the interlayer coupling is nearly constant because the stacking results in mismatched lattices over the entire sample. It follows that the Raman signature is relatively uniform. Note that for some samples, multiple breathing mode peaks appear, indicating nonuniform coupling across the interface. In contrast to the low-frequency interlayer modes, high-frequency intralayer Raman modes are much less sensitive to interlayer stacking and coupling. This research demonstrates the effectiveness of low-frequency Raman modes for probing the interfacial coupling and environment of twisted bilayer MoS2 and potentially other two-dimensional materials and heterostructures.

KEYWORDS: *Molybdenum disulfide, twisted bilayer, interlayer coupling, interlayer phonon modes, low-frequency Raman spectroscopy, density functional theory*
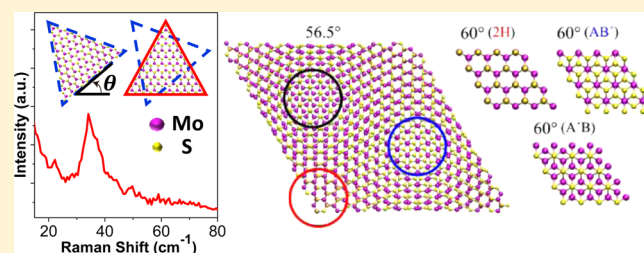
Molybdenum disulfide (MoS2) is a promising layered material for optoelectronic applications, mainly due to its strong photoluminescence (PL) emission,[1−4] light absorption,[1,4] photocurrent,[5,6] and valleytronics.[7−9] These properties can be very sensitive to the number of layers. For instance, the PL intensity of MoS2 drops dramatically going from a single-layer to few-layers,[1,2,10] due to the electronic structure changing from a direct to indirect bandgap.[2,10−14] Such a change underscores the importance of interlayer coupling in MoS2, which is sensitive to the layer−layer relative stacking. The attractiveness of bilayer compared to monolayer MoS2 for optical and electronic applications has been illustrated by the development of a MOSFET device where the optimal balance between carrier mobility and on/off ratio was achieved for bilayer systems,[15] as well as its unique spin and valley properties that are different from monolayer MoS2.[14,16,17] However, as previously reported in studies using PL spectroscopy,[10,18,19] the properties of bilayer MoS2 are sensitive to stacking due to the

high variability in possible interlayer coupling. This stacking sensitivity is expected to strongly affect the development of MoS2-based electronics.

Raman spectroscopy is a widely used technique to characterize nanomaterials due to its convenience, nondestructiveness, and sensitivity to materials change, including strain, temperature, doping, and defects. The Raman spectrum of MoS2 in the high-frequency (HF) region (E$_{2g}$ around 385 cm^{-1} and A$_{1g}$ around 405 cm^{-1}) has been extensively studied.[20−24] The low-frequency (LF) range (<50 cm^{-1}), where the interlayer in-plane shear and out-of-plane breathing modes (Figure 1 and Figure S1) originate from the relative vibrations between layers, has recently begun to attract increasing attention because these modes are more sensitive to both the interlayer coupling and
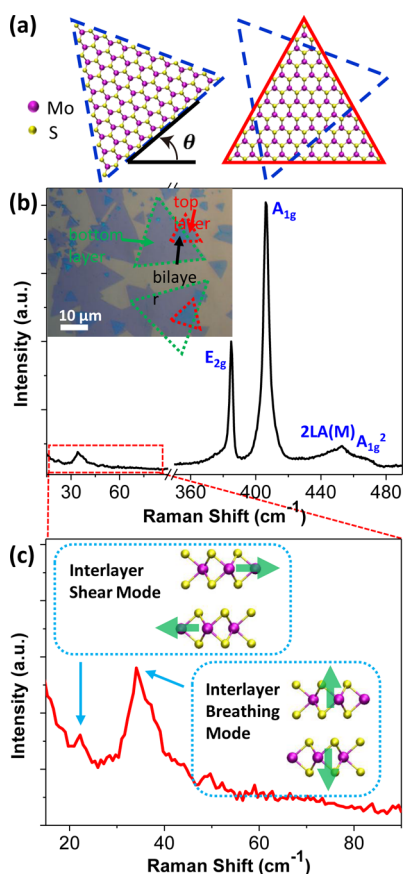
Figure 1. (a) Scheme of the angular twisting in bilayer MoS$_2$. The left and right plots show the separated top layer and bottom layer, respectively. Purple (yellow) spheres denote Mo (S) atoms. (b,c) Raman spectrum of twisted bilayer MoS$_2$ at θ = 46°. See panel (a) for definition of θ. (b) Full spectrum showing E$_{2g}$, A$_{1g}$, 2LA(M), and A$_{1g}^2$ modes of MoS$_2$. Inset: optical microscope image of a dry-transferred twisted bilayer sample. The green (red) triangles show the outlines of some bottom (top) layer MoS$_2$ triangles, and one bilayer region is labeled. The LF range is marked with a red dashed rectangle and is enlarged in panel (c), including interlayer shear and breathing modes. Their vibrational motions are shown in the insets of panel (c). Green arrows indicate the vibrational directions of each layer.

number of layers.[25,26] LF modes can also effectively probe the thickness-dependent interlayer coupling in other two-dimensional (2D) material systems, such as few-layer graphene and black phosphorus.[27−33] In addition to their capability to determine thickness, the interlayer shear and breathing modes have been used to uncover the relationship between interface coupling and stacking pattern in twisted multilayer graphene.[34−36] The LF modes show a unique fingerprint for the two most stable stacking configurations (i.e., 2H and 3R) in chemical vapor deposition (CVD) grown bilayers and trilayers of MoSe$_2$ and WSe$_2$. In contrast to the HF modes, which are almost unaffected by stacking, this LF sensitivity enables a clear determination of layer stacking.[37−39] However, most of the previous studies were limited to a few high-symmetry stacking patterns at 0° or 60°.[25,37] Therefore, except for a recent experimental study mainly on MoSe$_2$/MoS$_2$ heterobilayers,[40] a systematic LF Raman study on transition metal dichalcogenides (TMDs) to reveal the evolution of interlayer stacking and coupling within the full range of twisting angles is still needed.

Here, we report an integrated experimental/theoretical investigation of the interlayer shear and breathing modes of twisted bilayer MoS$_2$ from 0° to 60°. The Raman measurements reveal that these modes change notably with twisting, suggesting their sensitivity to interlayer stacking and coupling. Our first-principles density functional theory (DFT) calculations provide a detailed microscopic picture of how the interlayer stacking and coupling evolve with twisting. We find that when the twisting angle is near 0° or 60°, the frequencies and intensities of the shear and breathing modes strongly vary, showing a frequency shift of up to 8 cm^{-1} and an intensity change by as much as a factor of 4.8. This behavior is due to the mixture of multiple high-symmetry stackings near 0° or 60°, leading to significant changes in the stacking and interfacial coupling upon twisting. In contrast, for twisting angles between 20° and 40° where the stacking is found to yield mismatched lattices without any highly ordered domains, the shear mode cannot be observed, because its effects are expected at very low frequency (below 10 cm^{-1}). Here we use the concept of mismatched lattices wherever the resulting bilayer structure does not show any evident patches of high-symmetry stacking. The appearance of very low frequency spectral features for twisting angles between 20° and 40° is because in-plane layer–layer shear vibrations lead to virtually no restoring forces associated with the mismatched stacking (i.e., very weak interlayer shear coupling). The out-of-plane breathing mode shows small variations with different twisting angles, as the mismatched stacking leads to an almost constant interlayer breathing mode coupling. For some flakes, we observe the appearance of multiple breathing modes. This observation indicates the presence of a nonuniform interlayer coupling across the interface, probably caused by either multiple high-symmetry stacking patches or mechanical transfer-induced localized strains, defects, or wrinkles. This signature is particularly important for the characterization of samples used in a number of optoelectronic applications, which require highly uniform materials.

In contrast to the LF interlayer Raman modes, the HF modes are found to be much less sensitive to interlayer stacking and coupling; the maximum variation in frequency is found to be about 1 cm^{-1}. It follows that LF Raman modes are required to probe the interlayer stacking and coupling of twisted bilayer MoS$_2$, and they are best suited to reveal the interfacial qualities, such as the degree of nonuniformity. These results can be extended to other 2D materials and their heterostructures. With the growing interest in the mechanical stamping of monolayers to create a variety of van der Waals (vdW) homostructures and heterostructures for diverse electronic and optical applications,[41−44] LF Raman spectroscopy can be critical for understanding and characterizing the interfacial properties of layered materials.

We used the dry transfer method to stack two CVD monolayers together to prepare twisted bilayer MoS$_2$ samples (Figure 1a). This method is simple and effective, and allows preparation of samples with controllable twisting angles. In addition, this stacking method does not introduce any contaminating substances between the two layers. These properties ensure a robust and reproducible interlayer coupling.[10] The inset to Figure 1b shows an illustrative optical microscope image of twisted bilayer MoS$_2$ after dry transfer on a SiO$_2$/Si substrate. The bilayer area can be readily distinguished. Optical microscopy can detect the twisting angle θ but not the detailed stacking pattern and interfacial coupling strength. In contrast, and as will be shown here, LF Raman spectroscopy is a particularly well-suited technique to
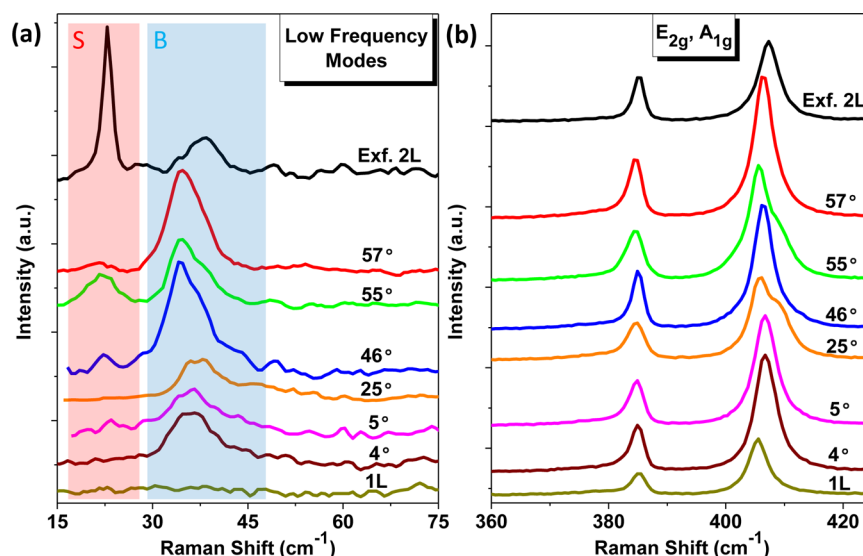
Figure 2. Raman spectra of twisted bilayer MoS_2 with different twisting angles selected from 0° to 60° and of monolayer (1L) and exfoliated bilayer MoS_2 (Exf. 2L). (a) The LF range including interlayer shear and breathing modes, and (b) the HF (high-frequency) range including E_{2g} and A_{1g} modes. In panel a, the red rectangle and letter "S" label the interlayer shear modes, and the blue rectangle and letter "B" label the interlayer breathing modes.
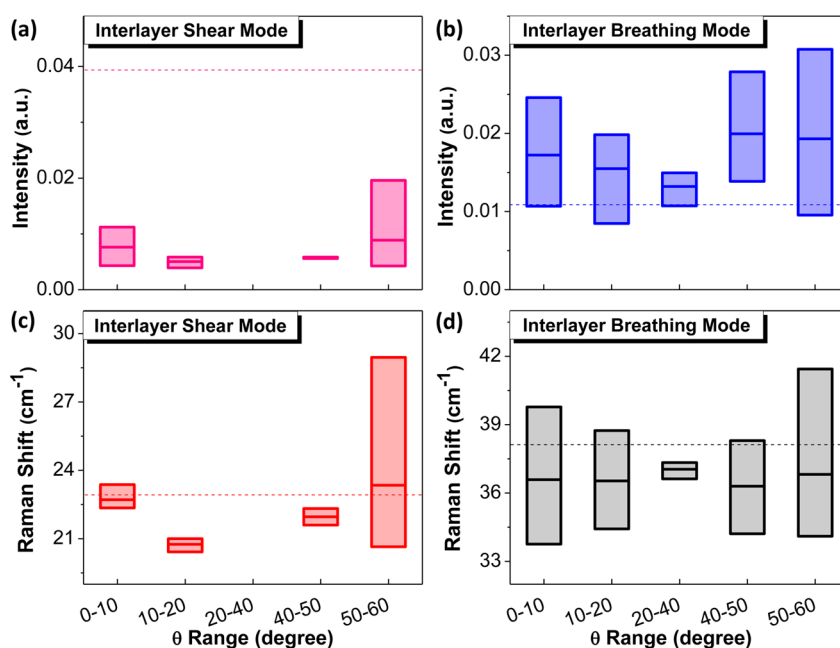

Figure 3. Twisting angle θ dependence of the LF interlayer Raman modes. θ dependence of the intensities of (a) shear modes located around 23 cm^{-1} and (b) breathing modes located around 37 cm^{-1}. θ dependence of the frequencies of (c) shear modes and (d) breathing modes. The θ values are categorized into five ranges. The heights of the data bars show the variation range of the data points in each θ range, and the horizontal line in the middle of each bar shows the mean value in the θ range. The values measured for exfoliated bilayer MoS_2 are labeled as the horizontal dashed lines in (a−d) for comparison.

determine these properties. Figure 1b shows a typical Raman spectrum in the frequency range of 15−490 cm^{-1} for a bilayer MoS_2 with $\theta = 46°$. In the HF range, the characteristic first-order E_{2g} and A_{1g} modes,[21] second-order 2LA(M) mode and first-order A_{1g}^2 mode[43] of MoS_2 can be seen. Note that strictly speaking, the symmetry assignments here are valid only for the bulk 2H stacking, while the symmetry assignments of a bilayer system can be changed with the stacking and twisting (Table S1). But for simplicity and consistency, the notations of E_{2g} and A_{1g} are used for all twisted bilayer systems (more details in Figure S1).

Distinctive Raman signals are also present in the LF range (<50 cm^{-1}). Zooming into this range (Figure 1c), there are two peaks corresponding to the interlayer shear and breathing modes.[25,26] As shown in the insets to Figure 1c, the LF interlayer modes describe the layer−layer vibrations with each layer moving as a whole unit, and hence their frequencies are solely determined by the weak interlayer restoring forces and thus are typically below 100 cm^{-1}.[30] They are categorized into two types: the in-plane shear mode and the out-of-plane breathing mode.[46] On the other hand, the HF modes involve vibrations from intralayer chemical bonds (Figure S1), and thus
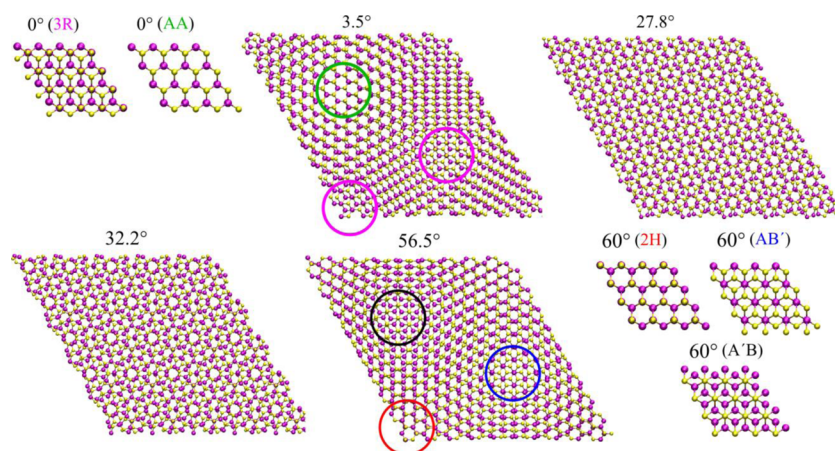
Figure 4. Atomic structures of commensurate bilayer MoS$_2$ at various twisting angles. Purple (yellow) spheres denote Mo (S) atoms. At $\theta = 0°$, there are two high-symmetry stacking patterns 3R and AA. When the system deviates from 0° slightly (e.g., 3.5°), both the 3R and AA stacking patches are still present, as highlighted by the purple and green circles, respectively. The boundary stackings between these high-symmetry patches serve as the transition to other stacking arragements. The patch sizes continuously decrease as θ deviates increasingly from 0°, and eventually the stacking becomes completely mismatched near 30° (e.g., 27.8°). At 60°, there are three high-symmetry stacking patterns, 2H, AB′, and A′B. When the system deviates slightly from 60° (e.g., 56.5°), 2H, AB′, and A′B stacking patches are still present, as highlighted by the red, blue, and black circles, respectively. The patch sizes continuously decrease with θ deviating more from 60°, and eventually the stacking becomes completely mismatched near 30° (e.g., 32.2°). More details are in Figures S5 and S7−S10.

the strong restoring forces are dominated by strong intralayer chemical bonds instead of the weak interlayer coupling. Because of the high sensitivity to the interface, the shear and breathing modes can be effectively used to probe the interlayer stacking and coupling.

Because of the D$_{3h}$ symmetry of monolayer MoS$_2$, the properties of twisted bilayer MoS$_2$ show a variation period of 60°.[10,18,19] The shear and breathing modes of MoS$_2$ bilayer with θ between 0° and 60° are shown in Figure 2a, together with the data from monolayer MoS$_2$ and exfoliated bilayer (2H stacked) MoS$_2$ presented for comparison. The interlayer shear and breathing modes are absent for monolayer MoS$_2$, further confirming that they originate from interlayer vibrations. For bilayer samples, the naturally 2H stacked (exfoliated sample) MoS$_2$ shows a sharp shear mode at 22.9 cm^{-1} and a broad breathing mode at 38.1 cm^{-1}, consistent with previous works.[25,26] Compared to exfoliated samples, experimentally stacked bilayers generally show shear modes with lower intensities and breathing modes with higher intensities, and both of these frequencies are down shifted. Different twisting angles also show different characteristics for the shear and breathing modes. The shear mode is typically of lower intensity than that of the breathing mode and is even absent for certain twisting angles. Similar phenomenon of the disappearance of the interlayer shear mode has also been observed in other bilayer TMD materials.[40] The frequency of the LF interlayer breathing mode also changes as a function of θ, shown in Figure 2a. In contrast to the LF interlayer Raman modes, the HF intralayer E$_{2g}$ and A$_{1g}$ Raman modes in Figure 2b show a much smaller dependence of their frequency and intensity as a function of θ, indicating that the HF modes are not as effective as the LF modes in detecting changes in stacking configurations.

We carefully studied the dependence of the shear and breathing modes on the twisting angles of bilayer MoS$_2$, and we extracted information for each Raman peak as a function of θ. The θ values are grouped into five ranges: 0°−10°, 10°−20°, 20°−40°, 40°−50°, and 50°−60°. In each θ range, the results for the statistical mean value and maximum variation for the

peak information are shown in Figure 3. Figure 3a,b shows the intensity dependence of each peak on each θ range. For both modes, when θ is close to 0° and 60°, the intensities show large variations, as indicated by the large bar heights. When θ approaches 30°, the shear mode disappears and the breathing mode intensities show only a weak dependence on θ, compared to the cases where θ is close to 0° or 60°. Hence the breathing mode has a smaller bar height in the [20°, 40°] range. The disappearance of the shear mode in the available frequency window between 20° and 40° is due to its extremely low frequencies (<10 cm^{-1}), as will be discussed below. For all the twisting angles, there is an intensity change of about a factor of 3.8 for the breathing mode and of about 4.8 times for the shear mode. The frequencies of the shear and breathing modes for different θ are shown in Figure 3c,d, respectively. The shear mode clearly disappears when θ is between 20° and 40°, while it shows up as θ approaches 0° or 60°. Similar to the intensity, the shear mode frequency near 0° or 60° varies significantly with θ (up to ~8 cm^{-1}). For the breathing mode, the frequency remains around 37 cm^{-1} when θ is between 20° and 40°, but varies by as much as 6.7 cm^{-1} when θ approaches 0° or 60°. Overall, both the intensities and frequencies of the shear and breathing modes show strong variations when θ is close to 0° or 60°, and they show considerably weaker variations when θ is between 20° and 40°, as is clearly shown in Figure 3 by the bar heights. For comparison purposes, we marked the parameters for exfoliated (naturally 2H stacked) bilayer MoS$_2$ with dashed lines in Figure 3. Compared to most twisted bilayer samples, the exfoliated sample shows a higher shear mode intensity, a lower breathing mode intensity, and relatively larger frequencies for both the shear and breathing modes. Such intensity and frequency differences can be attributed to the strong interlayer coupling of the naturally 2H stacking, as will be explained below.

It is interesting to note that some twisted flakes, such as for θ = 55° in Figure 2a and θ = 3°, 13°, 59°, and so forth in Figure S2, have asymmetric breathing modes, suggesting the possibility of overlapping of multiple modes. These multiple peaks also exist in the corresponding anti-Stokes spectra. For bilayer MoS$_2$
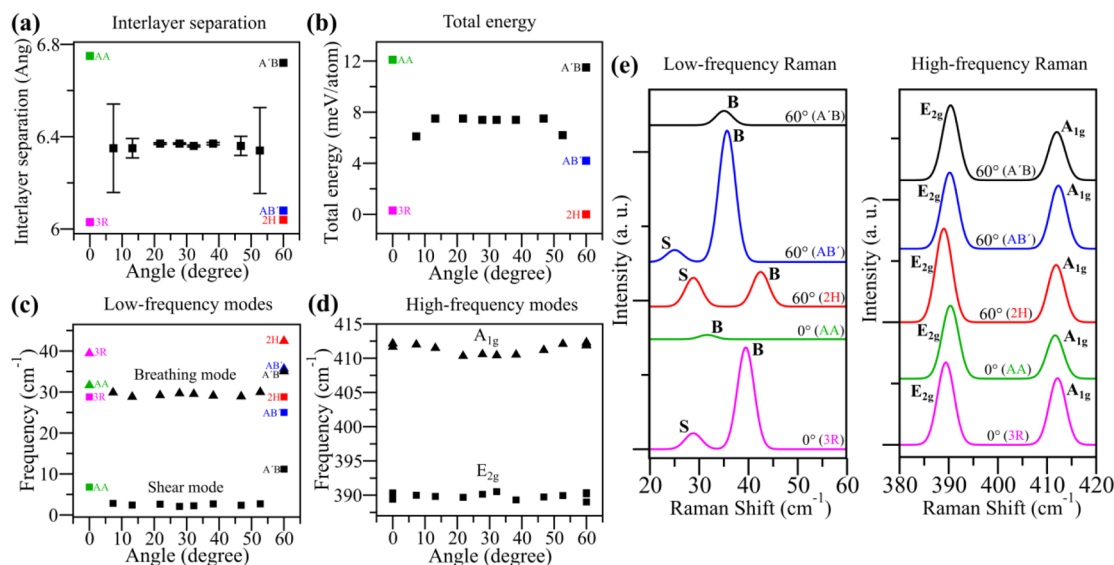
Figure 5. DFT calculations for twisting angles θ from 0° to 60°. (a) Average interlayer separation between the two Mo layers. The bars show the minimal and maximal local layer separations at an angle. (b) Total energy versus θ. The energy of 60° (2H stacking) bilayer is set as zero. (c) The θ dependence of the frequencies of LF shear mode (squares) and breathing mode (triangles). (d) The θ dependence of the frequencies of HF E_{2g} (squares) and A_{1g} (triangles) modes. In (a−d), both stackings 3R and AA are included at 0° (hence two data points at 0°), and all three stackings 2H, AB′ and A′B are included at 60° (hence three data points at 60°). In (a−c), these data points are differentiated by colors and labels, while in (d) they almost overlap. (e) Simulated Raman spectra of the five high-symmetry stackings at 0° and 60°. From (c−e), the LF Raman modes clearly show much larger frequency and intensity changes versus the stacking and twisting angle, compared to the HF Raman modes. All numerical data are also shown in Table S3.

with a uniform interface, there should be only one breathing mode. The presence of multiple breathing modes could arise from a nonuniform interface across which the interlayer distance and coupling vary significantly. For θ near 0° or 60°, different high-symmetry stacking patches coexist (Figure 4), which could lead to multiple breathing mode peaks, because each stacking patch contributes a different breathing mode, which will be discussed in detail below. In contrast, for θ near 30° where the stacking does not show any obvious high-symmetry patches, the presence of multiple peaks could be caused by localized strains, defects, or wrinkles, introduced during the dry transfer procedure (such effects could be possible for θ near 0° or 60° as well).[18] In short, LF Raman spectroscopy could provide a sensitive tool to detect the presence of nonuniform interface. It is well established that strains can affect the Raman spectrum of MoS_2.[47−49] In particular, LF interlayer Raman modes are very sensitive to the interlayer distance and coupling. Local strains introduced during the transfer process could lead to local variations of interlayer distance and coupling. Subsequently, multiple LF Raman peaks with different frequencies can appear. However, it is difficult to conclude that such phenomena are only due to strains instead of other localized effects. Strains on mono- or few-layer MoS_2 lead to a notable frequency shift of the high-frequency E_{2g} peak: $\Delta\omega/\epsilon$ is up to −2 cm^{-1} per percent of uniaxial tensile strain and 3 cm^{-1} for a 0.2% biaxial compressive strain, respectively. For the high-frequency A_{1g} peak, there is almost no frequency shift for the uniaxial strain, and the frequency shift can be about 2 cm^{-1} for a 0.2% biaxial compressive strain.[47−49] However, our measurements covering the whole θ range [0°, 60°] show that the variations of the E_{2g} and A_{1g} frequencies are within ∼1 cm^{-1} (will be discussed below), indicating that strains are not significant in the samples. Therefore, we expect that strains, though present, are not a dominating factor.

In addition to the LF shear and breathing modes, we also summarize how HF intralayer Raman modes (E_{2g}, A_{1g}, 2LA(M) and A_{1g}^{2}) change upon twisting. The frequencies of HF modes barely change. For instance, the A_{1g} mode is red-shifted from 0° (or 60°) to 30°, but the frequency change is only around 1 cm^{-1}, as shown in Figure S3a. For some flakes, the A_{1g} peak splits (Figure S3b), and multiple peaks can be observed in the LF range as well, suggesting that the A_{1g} splitting and the multiple LF modes share the same origin, namely, the presence of a nonuniform interface. The number of flakes featuring multiple LF interlayer modes is more than twice that of flakes with A_{1g} splitting, clearly indicating that the LF modes are more sensitive to interfacial environment than the HF modes. The variation of the E_{2g} frequency (Figure S3c) is also within about 1 cm^{-1}. The 2LA(M) mode around 452 cm^{-1} shown in Figure 1b is a second-order Raman mode involving two longitudinal acoustic (LA) phonons at the M point of the Brillouin zone.[45] Moreover, the A_{1g}^{2} mode in bilayer MoS_2,[25,45] located around 466 cm^{-1}, corresponds to the Raman inactive B_{2g} mode in bulk MoS_2, which becomes Raman active in few-layer MoS_2 due to symmetry breaking (see its vibration in Figure S1). For 2LA(M) and A_{1g}^{2} modes, the dependence of their frequencies on θ is also weak (Figure S3d). In short, the HF Raman modes are less effective than the LF ones to probe the interface. Finally, we note that for all of these HF intralayer Raman modes, relatively strong variations also occur when θ is close to 0° or 60°. This phenomenon is consistent with the experimental results for the LF modes, suggesting that the variation of interlayer coupling near 0° or 60° is the strongest and most complex.

To understand the experimental data in more detail, we first examined the atomic structures of twisted bilayer MoS_2 to reveal the microscopic picture of the stacking evolution with twisting. Unlike bilayer graphene that has two high-symmetry stacking patterns AB (i.e., Bernal) and AA, bilayer MoS_2 has

five high-symmetry stacking patterns due to its two different elements, as shown in Figures 4 and S5.[19,37,50,51] At $\theta = 0°$, there are two stacking patterns interchangeable by translation, 3R and AA. For 3R, Mo is over S and the other Mo and S are over the center of the hexagons; for AA, Mo is over Mo and S is over S. At $\theta = 60°$, there are three stacking configurations that are interchangeable by translation: 2H, AB′, and A′B. For 2H, Mo is over S and S is over Mo; for AB′, Mo is over Mo and all S are over the center of the hexagons; for A′B, S is over S and all Mo are over the center of the hexagons (more details provided in Figure S5). Note that 2H at 60° (also denoted as AA′) is the most stable configuration, and 3R at 0° (also denoted as AB) is the second most stable. These two stackings are present in natural and CVD-grown bilayer systems.[18,37] In the mechanically stacked samples, all five stacking patterns are possible and some of them coexist for the same twisting angle. In Figure 4, at 3.5° where the system slightly deviates from 0°, both 3R and AA stacking patches appear. The patch sizes where the AA and 3R configurations are seen continuously decrease as θ deviates more from 0°, and eventually the stacking becomes completely mismatched at 27.8° (more angles 1.8°, 7.3°, 13.2° and 21.8° are shown in Figure S7). On the other hand, at 56.5° where the system slightly deviates from 60°, the 2H, AB′, and A′B stacking patches all appear (Figure 4). Similar to the 0° case, the patch size continuously decreases as the deviation of θ from 60° increases, and eventually the stacking becomes completely mismatched at 32.2° (more angles 58.2°, 52.7°, 46.8°, and 38.2° in Figure S9). We also considered non-commensurate finite-size bilayer MoS$_2$ (Figures S8 and S10). Similar to Figure 4, when the system only slightly deviates from 0° or 60°, high-symmetry stacking configurations appear in roughly circular shapes. Their size continuously decreases, as θ deviates more from 0° or 60°. When $\theta > 10°$ and $\theta < 50°$, the high-symmetry stacking patches disappear, and the overall stacking becomes increasingly mismatched and does not display any high-symmetry domains.

DFT calculations were also carried out on various commensurate bilayer MoS$_2$ structures. We first examined the five high-symmetry stackings at 0° and 60°. As shown in Figure 5a,b and Table S3, 2H stacking is the most stable and all energies will be expressed relative to its energy. The 3R stacking shares a very similar interlayer separation and total energy (less stable by only 0.3 meV/atom).[47] Thus, the frequency of the shear mode is only weakly modified. The breathing mode is also mildly downshifted by 3 cm^{-1} from 2H to 3R (Figure 5c). Compared to 2H stacking, the interlayer distance of AB′ stacking slightly increases by 0.04 Å and the AB′ configuration becomes less stable by 4.2 meV/atom. Moving from 2H to AB′, the shear and breathing modes are slightly downshifted by 3.8 and 6.8 cm^{-1}, respectively. On the other hand, the interlayer distance of A′B (or AA) stacking is significantly increased by 0.68 (or 0.71) Å and these stacking configurations become much less stable by 11.5 (or 12.1) meV/atom, compared to 2H stacking.[19,50,51] This leads to dramatic frequency changes from 2H to A′B (or AA) stacking: the shear mode is down shifted by as much as 17.6 (or 22.0) cm^{-1} and the breathing mode by 7.4 (or 10.8) cm^{-1}. In stark contrast, the frequencies of the HF intralayer E$_{2g}$ and A$_{1g}$ modes are almost unchanged for all five high-symmetry stackings, where the maximum frequency variation is within 1−2 cm^{-1} (Figure 5d). These results clearly demonstrate that in-plane rotation and translation can induce different high-symmetry stackings for bilayer MoS$_2$ with considerable changes of the interlayer

distance and coupling. Such changes significantly modify LF Raman modes while HF modes are essentially unaffected.

In addition to shifts in frequencies, the intensity dependence of the LF Raman modes on stacking is also very noticeable, as shown in the simulated Raman spectra in Figure 5e. In contrast, the intensities of HF modes have a much weaker dependence on stacking. This result can be understood by the fact that Raman intensity of a phonon mode is positively correlated with the change of the system's electric polarizability by the corresponding phonon vibration.[39,52] For the HF modes corresponding to intralayer vibrations, the change of the polarizability (i.e., Raman intensity) is primarily contributed by the vibrations of intralayer chemical bonds. Hence, a change of layer−layer stacking results in a relatively small intensity change. In contrast, for the LF modes corresponding to layer−layer vibrations, the change of the polarizability is solely due to layer−layer vibrations. Thus, the change of layer−layer stacking can lead to a relatively dramatic intensity change, as seen in Figure 5e. Interestingly, in going from the 2H to 3R stackings in bilayer MoS$_2$, the intensity of the shear mode decreases while the intensity of the breathing mode increases (this effect was also experimentally observed in bilayer WSe$_2$),[37] and a similar intensity trend occurs for the 2H to AB′ transition. The 3R and AB′ stackings share similar interlayer coupling strength with 2H stacking, so their intensity changes are largely due to the altered atomic arrangements and different electronic environments for each atom. On the other hand, for A′B or AA stacking, as the interlayer distance is much larger (close to decoupling of the two layers) the layer−layer vibrations lead to a much smaller polarizability change, and hence the shear mode has almost zero intensity and the breathing mode has considerably weaker intensity.

Turning to θ near 0° or 60°, the stacking yields a pattern composed of a mixture of multiple high-symmetry domains. For 52.7°, bilayer MoS$_2$ has 2H, AB′, and A′B stacking patches, which have quite different interlayer separations from one another. Consequently, notable variations in the local interlayer distance (about 0.37 Å in Figure 5a) are expected. A similar variation of the local interlayer distance is found in the 7.3° sample because it has 3R and AA stacking patches with very different interlayer separations.[18] When the system deviates slightly from the natural 2H stacking at 60°, AB′ and A′B stacking patches appear. The shear mode intensity is considerably decreased for both AB′ and A′B stackings but the breathing mode intensity increases significantly for AB′ stacking (Figure 5e). Hence, compared to exfoliated 2H bilayer, generally for θ near 60°, the shear mode becomes weaker while the breathing mode is enhanced, largely due to the appearance of twisting-related AB′ and A′B stackings (such as at 57° and 55° in Figure 2 and more twisting angles shown in Figure S2). For the bilayer system near 0°, 3R and AA stacking patterns appear. Both exhibit weakened shear modes while 3R stacking has an enhanced breathing mode, compared to 2H stacking (Figure 5e). Hence, relative to the exfoliated 2H bilayer, generally for θ near 0°, the shear mode is weak while the breathing mode can be enhanced owing to the presence of 3R stacking (such as the 4° and 5° in Figure 2 and more angles shown in Figure S2). This analysis can explain why for $\theta < 10°$ or $\theta > 50°$ the average intensity of the shear mode is lower while that of the breathing mode is higher, compared to the exfoliated bilayer (Figure 3a,b). Regarding the frequencies, because all other stacking configurations have weaker interlayer coupling than the 2H stacking, the average frequencies of the

shear and breathing modes are generally lower compared to the exfoliated bilayer (Figure 3c,d). Besides, for $\theta < 10°$ or $\theta > 50°$ the coexisting high-symmetry stacking patches can lead to very different frequencies and intensities for the shear and breathing modes (Figure 5e and Table S3). Twisting can change both the weight of each stacking patch and the boundary stacking between the patches in the overall stacking pattern, and such changes will in turn modify their relative contributions to the Raman scattering. Therefore, the frequency and intensity variations of the shear and breathing modes can be large at different θ near 0° or 60°, as indicated by long bar heights in Figure 3 (frequency variation up to 8 cm^{-1} and intensity variation by 4.8 times).

The situation is different for θ in the $[20°, 40°]$ range, where the stacking is such that it does not present any sizable domains similar to those with high-symmetry stackings (Figure 4 and Figures S7−S10). It follows that neither rotation nor translation within this angular range change the coupling. This is confirmed by DFT calculations which show that the interlayer distance remains ∼6.36 Å with essentially no variation (Figure 5a) and the total energy varies negligibly (Figure 5b). Hence, the interlayer coupling is nearly constant, and consequently the frequency and intensity variations of the breathing mode in the $[20°, 40°]$ range are insignificant (short bar heights in Figure 3). Furthermore, compared to 2H stacking, the interlayer distance near 30° increases by 0.32 Å and the structure is energetically less stable by ∼7.4 meV/atom, suggesting much weaker interlayer coupling. Thus, the breathing mode frequency is lower than that of the exfoliated 2H bilayer, as shown in Figure 3d. Note that the shear mode cannot be observed in $[20°, 40°]$ since it has a calculated frequency as low as ∼2 cm^{-1} (Figure 5c and Table S3). This frequency is buried in the strong Rayleigh line and therefore beyond the detection limit available to Raman measurements. Such stark contrast between the shear and breathing modes originates from the mismatched stacking. The absence of local high-symmetry domains makes the stacking features essentially insensitive to the in-plane shear motion, leading to very small overall restoring force. In contrast, the out-of-plane breathing motion changes the interlayer distance and coupling and always leads to a finite overall restoring force.[36,40] To provide further evidence for these conclusions, we introduced artificial in-plane and out-of-plane relative shifts by 0.5 Å to the bilayer systems for various stackings and angles (Figure S11 and Table S4). Compared to 2H stacking where the in-plane shift gives energy difference of 3.62 meV/atom, the in-plane shift results in almost no energy difference for 21.8°, 27.8°, 32.2°, and 38.2° (only ∼0.05 meV/atom), confirming the very low restoring force from the in-plane shear motion for these mismatched stacking arrangements. However, the out-of-plane shifts lead to comparable magnitudes of energy differences for different stackings and angles. Clearly, the shear mode is overall more sensitive to twisting and it might provide a good indicator of the degree of stacking mismatch, while the breathing mode is present for all twisting angles and thus serves as a practical indicator of the interlayer coupling for mechanically stacked systems.

Finally, for θ in the $[10°, 20°]$ or $[40°, 50°]$ ranges the predicted local stacking arrangements lie between the high-symmetry stacking mixture near 0° or 60° and the mismatched stacking near 30°, and it follows that the θ dependence of the shear and breathing modes is intermediate (Figure 3). Note that there is a seemingly appreciable discrepancy between the

measured (Figure 3c) and calculated (Figure 5c) values of the shear mode in the $[10°, 20°]$ or $[40°, 50°]$ ranges, where the measured frequencies are around 21−22 cm^{-1} while the calculated ones are around 2−3 cm^{-1}. At these angles, an ideal interface has largely mismatched stacking arrangements without high-symmetry stacking patches, and our calculations suggest that little restoring force can come from the in-plane shear motion (thus frequency 2−3 cm^{-1}). However, the presence of various nonideal effects (such as local strains, wrinkles, or defects) can in actuality induce shorter interlayer distance locally, and thus the shear mode with relatively stronger restoring force and higher frequencies can appear (like frequency 21−22 cm^{-1}). If a sample has little or no nonideal effects, the shear mode should disappear. In fact, only less than half of the samples in the $[10°, 20°]$ or $[40°, 50°]$ ranges show the shear mode experimentally. This suggests that localized strains, wrinkles, or defects are probably present in these samples to cause the measured 21−22 cm^{-1} modes, while the majority of the samples are free of these nonideal effects and thus the shear mode has too low a frequency to be observable as the theory predicts.

To quantify the strengths of interlayer shear and breathing coupling, we estimated their force constants based on the widely used linear chain model (see Section S1, Figure S4, and Table S2 in Supporting Information).[25−27,53] The force constant of the shear mode (K_s) was found to vary from 2.30 × 10^{19} to 4.51 × 10^{19} N/m^3 in the range of $\theta < 20°$ and $\theta > 40°$, where the shear mode is observable. This gives a variance of 0.2 × 10^{19} N/m^3 and a relative deviation of ∼7.2%. Note that the shear mode disappears in the $[20°, 40°]$ range due to its extremely low frequency (only ∼2 cm^{-1} according to DFT calculations). Hence, in $[20°, 40°]$, K_s is estimated to be about 0.02 × 10^{19} N/m^3, and thus the relative deviation in the whole range $[0°, 60°]$ is very large (up to more than 90%). However, the force constant of the breathing mode (K_b) ranges from 6.26 × 10^{19} to 9.52 × 10^{19} N/m^3 in $[0°, 60°]$, giving a variance of 0.43 × 10^{19} N/m^3 and relative deviation of 5.9%, which is much smaller than the variation of K_s. The strengths of the interlayer coupling are generally 2 orders of magnitude smaller than those of the intralayer vibrations (the force constants of E$_{2g}$ and A$_{1g}$ modes are 1.88 × 10^{21} and 3.46 × 10^{21} N/m^3, respectively).[28]

In conclusion, we have systematically investigated the interlayer stacking and coupling in twisted bilayer MoS$_2$ using a combination of LF Raman spectroscopy and first-principles DFT calculations. Our results show that in-plane rotation and translation can induce five different high-symmetry stacking patterns at 0° (3R and AA) and 60° (2H, AB′, and A′B) with substantially different interlayer distances and coupling strengths. Consequently, the frequencies and intensities of the LF interlayer shear and breathing modes change dramatically with stacking. Upon twisting away from 0° and 60°, the stacking becomes a mixture of these high-symmetry stacking patterns, and thus twisting leads to significant changes in stacking and coupling, as reflected by notable frequency and intensity variations of the shear and breathing modes (frequency variation by 8 cm^{-1} and intensity variation by 4.8 times). On the other hand, when θ is within $[20°, 40°]$, the coupling is nearly constant because the stacking pattern shows highly mismatched lattices with no local high-symmetry domains. This explains why the breathing mode shows small variations in such θ range. Interestingly, the shear mode disappears near 30°, as the in-plane shear motion leads to almost no restoring force from the mismatched stacking and its

frequency is close to zero. Moreover, a nonuniform interface with variable interlayer coupling can be formed due to the coexistence of multiple high-symmetry stacking patches, or mechanical stamping induced localized strains, defects, or wrinkles. Such nonuniformity can be properly captured by LF Raman spectroscopy (i.e., multiple breathing modes). This work paves the way toward a deeper understanding of interfacial properties of 2D homostructures and heterostructures and proves that LF Raman spectroscopy offers effective and quick characterization of layered materials.

Methods. *CVD and Dry Transfer of MoS₂.* MoS_2 monolayers were synthesized by chemical vapor deposition (CVD) using the seeding promoter method.[54] In our synthesis, the precursors, molybdenum trioxide (MoO_3) and sulfur (S), were loaded in two crucibles separated in the quartz tube. A 300 nm SiO_2/Si substrate was placed face-down on the crucible loaded with MoO_3. The seeding promoter, perylene-3,4,9,10-tetracarboxylic acid tetrapotassium salt (PTAS), was applied on the substrate surface. Under the growth temperature (650 °C), MoO_3 and S react and form MoS_2. With the assistance of the seeding promoter, monolayer MoS_2 flakes with triangle domain shapes were nucleated and deposited on the substrate. The MoS_2 crystalline orientation can be identified from the triangle domain shapes:[55] the triangles with straight edges have Mo-terminated zigzag edges.

The dry transfer method used to stack two MoS_2 monolayers and form twisted bilayer MoS_2 has been published in our previous work.[10] Briefly, monolayer CVD MoS_2 flakes on a SiO_2/Si substrate were used. The MoS_2 chip was spin coated with 4.5% poly(methyl methacrylate) (PMMA), followed by substrate etching using potassium hydroxide (KOH) solution. Then a polydimethyl-siloxane (PDMS) elastomer was used to load the PMMA-MoS_2 film with PMMA touching PDMS. The structure was placed under an optical microscope connected with a motorized stage. The MoS_2 layer was facing down, and another substrate with MoS_2 flakes was placed underneath. By adjusting the relative locations and angles between the top and bottom MoS_2 flakes through the optical microscope, the PDMS structure on top was lowered to have the two MoS_2 layers contacting each other. After subsequent 130 °C baking, the PDMS was carefully lifted, leaving the top layer MoS_2 still on the SiO_2/Si substrate. Therefore, twisted bilayer MoS_2 was constructed on a SiO_2/Si substrate. The PMMA left on the substrate was then removed by annealing in an Ar atmosphere in 400 °C for 3 h. This dry transfer method introduces no foreign substance between the two layers of MoS_2, ensuring strong interlayer coupling.[10] Atomic force microscopy and PL spectroscopy have been measured on the twisted bilayer MoS_2 and have confirmed that the interface has no foreign substances.[10] The AFM shows the surface is relatively uniform and the interlayer distance is similar to the thickness of monolayer MoS_2. PL shows that bilayer area has weaker PL intensity than monolayer area. This is an indication of coupling between the top and bottom layers and has also been reported in literatures.[1,2,18] In contrast, for a control sample that contains some PMMA residues in between the two layers, the bilayer area has stronger PL intensity than monolayer area.[10] Optical microscopy was used to identify the twisting angle between the top and bottom layers of MoS_2.

Raman Measurements. Raman spectra were taken in a backscattering configuration on a triple Raman spectrometer (T64000, Horiba Jobin-Yvon) equipped with three 1800 lines/mm gratings. The excitation laser was a frequency-doubled diode pumped solid state laser (Excelsior, Spectra Physics) with the wavelength of 532.1 nm. The laser power on the sample was maintained at 120 μW to avoid damage to the sample. The typical acquisition time was 300 s to ensure a high signal-to-noise ratio. A 100× objective with NA = 0.95 was used to focus the laser beam to a spot ∼1 μm in diameter on the sample surface. A motorized XYZ stage with micron resolution was used to locate MoS_2 flakes. Both Stokes and anti-Stokes Raman spectra were collected. The Raman spectra were fit with Lorentzian line shape to extract peak information. More than 50 samples covering the whole [0°, 60°] twisting angle range were measured.

DFT Calculations. Plane-wave DFT calculations were performed using the VASP package[56] equipped with the projector augmented-wave (PAW) method for electron−ion interactions. The local density approximation (LDA) was adopted for the exchange-correlation interaction with the energy cutoff set at 400 eV.[10,18,25,37] For bulk MoS_2, both atoms and cell volumes were allowed to relax until the residual forces were below 0.001 eV/Å. We used a 24 × 24 × 4 k-point sampling in the Monkhorst−Pack scheme.[57] The bilayer MoS_2 systems were modeled by a periodic slab geometry using the optimized in-plane lattice constants of the bulk. For the five high-symmetry stackings (corresponding to 0° or 60°, see Figures 4 and S5), a 24 × 24 × 1 k-point sampling was used since their in-plane lattice constants are the same as for the bulk a = 3.13 Å. We also considered other twisting angles with commensurate structures (i.e., periodic boundary condition can be applied in the in-plane directions and a unit cell can be located), as shown in Figure S6. Specifically, for 21.8° and 38.2°, the in-plane lattice constants are 8.29 Å and a 9 × 9 × 1 k-point sampling was used; for 27.8° and 32.2°, the in-plane lattice constants are 11.29 Å and a 6 × 6 × 1 k-point sampling was used; for 13.2° and 46.8°, the in-plane lattice constants are 13.65 Å and a 6 × 6 × 1 k-point sampling was used; for 7.3° and 52.7°, the in-plane lattice constants are 24.41 Å and a 1 × 1 × 1 k-point sampling was used. For all bilayer systems, a vacuum region of at least 18 Å in the z-direction normal to the plane was used to avoid spurious interactions with replicas, and all atoms were relaxed until the residual forces were below 0.001 eV/Å. Then nonresonant Raman calculations were performed on the five relaxed high-symmetry stackings at 0° or 60° using the PHONON software[58,59] based on the finite difference scheme (more details in refs 37 and 52).

■ ASSOCIATED CONTENT

ⓢ Supporting Information

The Supporting Information is available free of charge on the ACS Publications website at DOI: 10.1021/acs.nanolett.5b05015.

Linear chain model, figures of vibrational illustrations of MoS_2 Raman modes, low-frequency Raman spectra of twisted bilayer MoS_2 with different twisting angles, twisting angle dependence of the interlayer vibration force constants, twisting angle dependence of the high-frequency modes, five high-symmetry stacking patterns at 0° and 60°, and illustrations of the interlayer stacking evolution with the twisting angle, tables of force constants (K_b, K_s) of twisted bilayer MoS_2, and DFT calculations of bilayer MoS_2 at different twisting angles. (PDF)

■ AUTHOR INFORMATION

Corresponding Authors
*(X.L.) E-mail: xiling@mit.edu. Tel: +1-617-253-6860.
*(V.M.) E-mail: meuniv@rpi.edu. Tel: +1-518-276-6886.
*(M.S.D.) E-mail: millie@mgm.mit.edu. Tel: +1-617-253-6864.

Author Contributions

S.H., L.L., and X.L. contributed equally to this work.

S.H., L.L., X.L., J.K., and M.S.D. initiated the project. S.H., X.L., and A.A.P. performed the experiment and analyzed the data. L.L. and V.M. contributed to the theoretical calculations. S.H., L.L., and X.L. wrote the paper. All the authors discussed the results and revised the paper.

Notes

The authors declare no competing financial interest.

■ ACKNOWLEDGMENTS

■ REFERENCES

(1) Mak, K. F.; Lee, C.; Hone, J.; Shan, J.; Heinz, T. F. *Phys. Rev. Lett.* **2010**, *105*, 136805.
(2) Splendiani, A.; Sun, L.; Zhang, Y.; Li, T.; Kim, J.; Chim, C.-Y.; Galli, G.; Wang, F. *Nano Lett.* **2010**, *10*, 1271−1275.
(3) Scheuschner, N.; Ochedowski, O.; Kaulitz, A.-M.; Gillen, R.; Schleberger, M.; Maultzsch, J. *Phys. Rev. B: Condens. Matter Mater. Phys.* **2014**, *89*, 125406.
(4) Eda, G.; Yamaguchi, H.; Voiry, D.; Fujita, T.; Chen, M.; Chhowalla, M. *Nano Lett.* **2011**, *11*, 5111−5116.
(5) Lopez-Sanchez, O.; Lembke, D.; Kayci, M.; Radenovic, A.; Kis, A. *Nat. Nanotechnol.* **2013**, *8*, 497−501.
(6) Yin, Z.; Li, H.; Li, H.; Jiang, L.; Shi, Y.; Sun, Y.; Lu, G.; Zhang, Q.; Chen, X.; Zhang, H. *ACS Nano* **2012**, *6*, 74−80.
(7) Mai, C.; Barrette, A.; Yu, Y.; Semenov, Y. G.; Kim, K. W.; Cao, L.; Gundogdu, K. *Nano Lett.* **2014**, *14*, 202−206.
(8) Zeng, H.; Dai, J.; Yao, W.; Xiao, D.; Cui, X. *Nat. Nanotechnol.* **2012**, *7*, 490−493.
(9) Xiao, D.; Liu, G.-B.; Feng, W.; Xu, X.; Yao, W. *Phys. Rev. Lett.* **2012**, *108*, 196802.
(10) Huang, S.; Ling, X.; Liang, L.; Kong, J.; Terrones, H.; Meunier, V.; Dresselhaus, M. S. *Nano Lett.* **2014**, *14*, 5500−5508.
(11) Jin, W.; Yeh, P.-C.; Zaki, N.; Zhang, D.; Sadowski, J. T.; Al-Mahboob, A.; van der Zande, A. M.; Chenet, D. a.; Dadap, J. I.; Herman, I. P.; Sutter, P.; Hone, J.; Osgood, R. M. *Phys. Rev. Lett.* **2013**, *111*, 106801.
(12) Cheiwchanchamnangij, T.; Lambrecht, W. R. L. *Phys. Rev. B: Condens. Matter Mater. Phys.* **2012**, *85*, 205302.
(13) Kormányos, A.; Zólyomi, V.; Drummond, N. D.; Rakyta, P.; Burkard, G.; Fal'ko, V. I. *Phys. Rev. B: Condens. Matter Mater. Phys.* **2013**, *88*, 045416.
(14) Jiang, T.; Liu, H.; Huang, D.; Zhang, S.; Li, Y.; Gong, X.; Shen, Y.-R.; Liu, W.-T.; Wu, S. *Nat. Nanotechnol.* **2014**, *9*, 825−829.
(15) Wang, H.; Yu, L.; Lee, Y.-H.; Shi, Y.; Hsu, A.; Chin, M. L.; Li, L.-J.; Dubey, M.; Kong, J.; Palacios, T. *Nano Lett.* **2012**, *12*, 4674−4680.
(16) Mak, K. F.; McGill, K. L.; Park, J.; McEuen, P. L. *Science* **2014**, *344*, 1489−1492.
(17) Wu, S.; Ross, J. S.; Liu, G.; Aivazian, G.; Jones, A.; Fei, Z.; Zhu, W.; Xiao, D.; Yao, W.; Cobden, D.; Xu, X. *Nat. Phys.* **2013**, *9*, 149−153.
(18) van der Zande, A. M.; Kunstmann, J.; Chernikov, A.; Chenet, D. A.; You, Y.; Zhang, X.; Huang, P. Y.; Berkelbach, T. C.; Wang, L.; Zhang, F.; Hybertsen, M. S.; Muller, D. A.; Reichman, D. R.; Heinz, T. F.; Hone, J. C. *Nano Lett.* **2014**, *14*, 3869−3875.
(19) Liu, K.; Zhang, L.; Cao, T.; Jin, C.; Qiu, D.; Zhou, Q.; Zettl, A.; Yang, P.; Louie, S. G.; Wang, F. *Nat. Commun.* **2014**, *5*, 4966.
(20) Li, H.; Zhang, Q.; Yap, C. C. R.; Tay, B. K.; Edwin, T. H. T.; Olivier, A.; Baillargeat, D. *Adv. Funct. Mater.* **2012**, *22*, 1385−1390.
(21) Lee, C.; Yan, H.; Brus, L. E.; Heinz, T. F.; Hone, J.; Ryu, S. *ACS Nano* **2010**, *4*, 2695−2700.
(22) Castellanos-Gomez, A.; Roldán, R.; Cappelluti, E.; Buscema, M.; Guinea, F.; van der Zant, H. S. J.; Steele, G. A. *Nano Lett.* **2013**, *13*, 5361−5366.
(23) Conley, H. J.; Wang, B.; Ziegler, J. I.; Haglund, R. F.; Pantelides, S. T.; Bolotin, K. I. *Nano Lett.* **2013**, *13*, 3626−3630.
(24) Shi, Y.; Huang, J.-K.; Jin, L.; Hsu, Y.-T.; Yu, S. F.; Li, L.-J.; Yang, H. Y. *Sci. Rep.* **2013**, *3*, 1839.
(25) Zhao, Y.; Luo, X.; Li, H.; Zhang, J.; Araujo, P. T.; Gan, C. K.; Wu, J.; Zhang, H.; Quek, S. Y.; Dresselhaus, M. S.; Xiong, Q. *Nano Lett.* **2013**, *13*, 1007−1015.
(26) Zhang, X.; Han, W. P.; Wu, J. B.; Milana, S.; Lu, Y.; Li, Q. Q.; Ferrari, A. C.; Tan, P. H. *Phys. Rev. B: Condens. Matter Mater. Phys.* **2013**, *87*, 115413.
(27) Tan, P. H.; Han, W. P.; Zhao, W. J.; Wu, Z. H.; Chang, K.; Wang, H.; Wang, Y. F.; Bonini, N.; Marzari, N.; Pugno, N.; Savini, G.; Lombardo, A.; Ferrari, A. C. *Nat. Mater.* **2012**, *11*, 294−300.
(28) Lui, C. H.; Heinz, T. F. *Phys. Rev. B: Condens. Matter Mater. Phys.* **2013**, *87*, 121404.
(29) Zhang, X.; Qiao, X.-F.; Shi, W.; Wu, J.-B.; Jiang, D.-S.; Tan, P.-H. *Chem. Soc. Rev.* **2015**, *44*, 2757−2785.
(30) Ling, X.; Liang, L.; Huang, S.; Puretzky, A. A.; Geohegan, D. B.; Sumpter, B. G.; Kong, J.; Meunier, V.; Dresselhaus, M. S. *Nano Lett.* **2015**, *15*, 4080−4088.
(31) Luo, X.; Lu, X.; Koon, G. K. W.; Castro Neto, A. H.; Özyilmaz, B.; Xiong, Q.; Quek, S. Y. *Nano Lett.* **2015**, *15*, 3931−3938.
(32) He, R.; Yang, J.-A.; Yin, Z.; Ye, Z.; Ye, G.; Cheng, J.; Li, J.; Lui, C. H. *Nano Lett.* **2016**, ASAP DOI: 10.1021/acs.nanolett.5b04925.
(33) Zhao, H.; Wu, J.; Zhong, H.; Guo, Q.; Wang, X.; Xia, F.; Yang, L.; Tan, P.; Wang, H. *Nano Res.* **2015**, *8*, 3651−3661.
(34) Wu, J.-B.; Zhang, X.; Ijäs, M.; Han, W.-P.; Qiao, X.-F.; Li, X.-L.; Jiang, D.-S.; Ferrari, A. C.; Tan, P.-H. *Nat. Commun.* **2014**, *5*, 5309.
(35) Cong, C.; Yu, T. *Nat. Commun.* **2014**, *5*, 4709.
(36) Wu, J.-B.; Hu, Z.-X.; Zhang, X.; Han, W.-P.; Lu, Y.; Shi, W.; Qiao, X.-F.; Ijäs, M.; Milana, S.; Ji, W.; Ferrari, A. C.; Tan, P.-H. *ACS Nano* **2015**, *9*, 7440−7449.
(37) Puretzky, A. A.; Liang, L.; Li, X.; Xiao, K.; Wang, K.; Mahjouri-Samani, M.; Basile, L.; Idrobo, J. C.; Sumpter, B. G.; Meunier, V.; Geohegan, D. B. *ACS Nano* **2015**, *9*, 6333−6342.
(38) Lu, X.; Utama, M. I. B.; Lin, J.; Luo, X.; Zhao, Y.; Zhang, J.; Pantelides, S. T.; Zhou, W.; Quek, S. Y.; Xiong, Q. *Adv. Mater.* **2015**, *27*, 4502−4508.
(39) Luo, X.; Lu, X.; Cong, C.; Yu, T.; Xiong, Q.; Ying Quek, S. *Sci. Rep.* **2015**, *5*, 14565.
(40) Lui, C. H.; Ye, Z.; Ji, C.; Chiu, K.-C.; Chou, C.-T.; Andersen, T. I.; Means-Shively, C.; Anderson, H.; Wu, J.-M.; Kidd, T.; Lee, Y.-H.; He, R. *Phys. Rev. B: Condens. Matter Mater. Phys.* **2015**, *91*, 165403.
(41) Hong, X.; Kim, J.; Shi, S.-F.; Zhang, Y.; Jin, C.; Sun, Y.; Tongay, S.; Wu, J.; Zhang, Y.; Wang, F. *Nat. Nanotechnol.* **2014**, *9*, 682−686.
(42) Lee, C.-H.; Lee, G.-H.; van der Zande, A. M.; Chen, W.; Li, Y.; Han, M.; Cui, X.; Arefe, G.; Nuckolls, C.; Heinz, T. F.; Guo, J.; Hone, J.; Kim, P. *Nat. Nanotechnol.* **2014**, *9*, 676−681.
(43) Ceballos, F.; Bellus, M. Z.; Chiu, H.-Y.; Zhao, H. *ACS Nano* **2014**, *8*, 12717−12724.
(44) Memaran, S.; Pradhan, N. R.; Lu, Z.; Rhodes, D.; Ludwig, J.; Zhou, Q.; Ogunsolu, O.; Ajayan, P. M.; Smirnov, D.; Fernández-

Domínguez, A. I.; García-Vidal, F. J.; Balicas, L. *Nano Lett.* **2015**, *15*, 7532−7538.

(45) Terrones, H.; Corro, E.; Feng, S.; Poumirol, J. M.; Rhodes, D.; Smirnov, D.; Pradhan, N. R.; Lin, Z.; Nguyen, M. A. T.; Elías, A. L.; Mallouk, T. E.; Balicas, L.; Pimenta, M. A.; Terrones, M. *Sci. Rep.* **2014**, *4*, 4215.

(46) Bhimanapati, G. R.; Lin, Z.; Meunier, V.; Jung, Y.; Cha, J.; Das, S.; Xiao, D.; Son, Y.; Strano, M. S.; Cooper, V. R.; Liang, L.; Louie, S. G.; Ringe, E.; Zhou, W.; Kim, S. S.; Naik, R. R.; Sumpter, B. G.; Terrones, H.; Xia, F.; Wang, Y.; Zhu, J.; Akinwande, D.; Alem, N.; Schuller, J. A.; Schaak, R. E.; Terrones, M.; Robinson, J. A. *ACS Nano* **2015**, *9*, 11509−11539.

(47) Wang, Y.; Cong, C.; Qiu, C.; Yu, T. *Small* **2013**, *9*, 2857−2861.

(48) Rice, C.; Young, R.; Zan, R.; Bangert, U.; Wolverson, D.; Georgiou, T.; Jalil, R.; Novoselov, K. *Phys. Rev. B: Condens. Matter Mater. Phys.* **2013**, *87*, 081307.

(49) Hui, Y. Y.; Liu, X.; Jie, W.; Chan, N. Y.; Hao, J.; Hsu, Y.-T.; Li, L.-J.; Guo, W.; Lau, S. P. *ACS Nano* **2013**, *7*, 7126−7131.

(50) He, J.; Hummer, K.; Franchini, C. *Phys. Rev. B: Condens. Matter Mater. Phys.* **2014**, *89*, 075409.

(51) Cao, B.; Li, T. *J. Phys. Chem. C* **2015**, *119*, 1247−1252.

(52) Liang, L.; Meunier, V. *Nanoscale* **2014**, *6*, 5394−5401.

(53) Kittel, C. *Introduction to Solid State Physics*, 8th ed.; Wiley: New York, 2004.

(54) Ling, X.; Lee, Y.-H.; Lin, Y.; Fang, W.; Yu, L.; Dresselhaus, M. S.; Kong, J. *Nano Lett.* **2014**, *14*, 464−472.

(55) van der Zande, A. M.; Huang, P. Y.; Chenet, D. a; Berkelbach, T. C.; You, Y.; Lee, G.-H.; Heinz, T. F.; Reichman, D. R.; Muller, D. a; Hone, J. C. *Nat. Mater.* **2013**, *12*, 554−561.

(56) Kresse, G.; Furthmüller, J. *Comput. Mater. Sci.* **1996**, *6*, 15−50.

(57) Monkhorst, H. J.; Pack, J. D. *Phys. Rev. B* **1976**, *13*, 5188−5192.

(58) Parlinski, K.; Li, Z. Q.; Kawazoe, Y. *Phys. Rev. Lett.* **1997**, *78*, 4063−4066.

(59) Parlinski, K. Computer Code PHONON, 2010, http://wolf.ifj. edu.pl/phonon/.